Mars Orbiter Laser Altimeter: receiver model and performance analysis

James B. Abshire, Xiaoli Sun, and Robert S. Afzal

The design, calibration, and performance of the Mars Orbiter Laser Altimeter (MOLA) receiver are described. The MOLA measurements include the range to the surface, which is determined by the laser-pulse time of flight; the height variability within the footprint determined by the laser echo pulse width; and the apparent surface reflectivity determined by the ratio of the echo to transmitted pulse energies.

OCIS codes: 280.3640, 280.3400, 120.1880, 350.6090, 040.6040, 120.0280.

1. Introduction

The Mars Orbiter Laser Altimeter (MOLA)[1–3] is one of the four instruments onboard NASA's Mars Global Surveyor (MGS) spacecraft.[4] Figure 1 shows a sketch of the MGS spacecraft and the MOLA instrument. The MOLA determines the distance from the MGS spacecraft to the Mars surface by measuring the time of flight of its laser pulses. The topographic height of the planet's surface at the laser footprint is then determined through the geometry of the planet radius, the spacecraft orbit altitude, and the pointing angle of the instrument. A simplified measurement geometry is shown in Fig. 2, and the specifications for the MOLA are given in Table 1.

The primary objective of the MOLA investigation is to determine the global topography of Mars at levels suitable for addressing fundamental questions in planetary geology and geophysics. Secondary objectives are to characterize the 1064-nm surface reflectivity of Mars, to contribute to analyses of global surface mineralogy and seasonal albedo changes, to assist in addressing problems in atmospheric circulation, and to provide geodetic control and topography for assessing future Mars landing sites.

Prior to the MOLA measurements, the heights and slopes of Mars topography were determined by photogrammetric analysis of the stereo image pairs from the Viking orbiters. However, there are many error sources in this approach, and smooth or cloudy regions are poorly suited for this technique. The resulting vertical errors in the pre-MOLA maps of Mars were as large as a few kilometers. Topographic profiles with meter-level accuracies are needed to understand the present shape of the Mars surface so as to infer the geophysical processes that shaped it during its history. Accurate height measurements are needed to study the relative altitude of surface features; to determine the height and volume of the icecaps, volcanoes, and craters; to determine the size, slope, and depth of drainage basins; and to detect evidence of hidden craters and possible ancient shorelines.

The range from the MGS spacecraft to the illuminated spot on the surface is related to the laser-pulse time of flight by

$$R_m = \frac{c\Delta T_{\mathrm{opt}}}{2}, \qquad (1)$$

with $c = 299{,}792{,}458$ m/s the vacuum speed of light.[5] Here we have neglected the effect of the atmospheric delay, which is only a few centimeters on Mars because of the low (4–6 mbars) surface pressure. The height of the surface at the laser footprint can be written as

$$h_s = [R_{\mathrm{MGS}}{}^2 + R_m{}^2 - 2R_m R_{\mathrm{MGS}} \cos(\phi)]^{1/2} - R_{\mathrm{ref}}, \quad (2)$$

where R_{MGS} is the radius of the MGS spacecraft orbit, ϕ is the pointing angle with respect to nadir, and R_{ref} is the radius of the reference surface of the planet, which is often taken to be the geoid.

The final accuracy of the surface height determination is governed by uncertainties in the spacecraft position, the pointing angle of the laser beam, and the
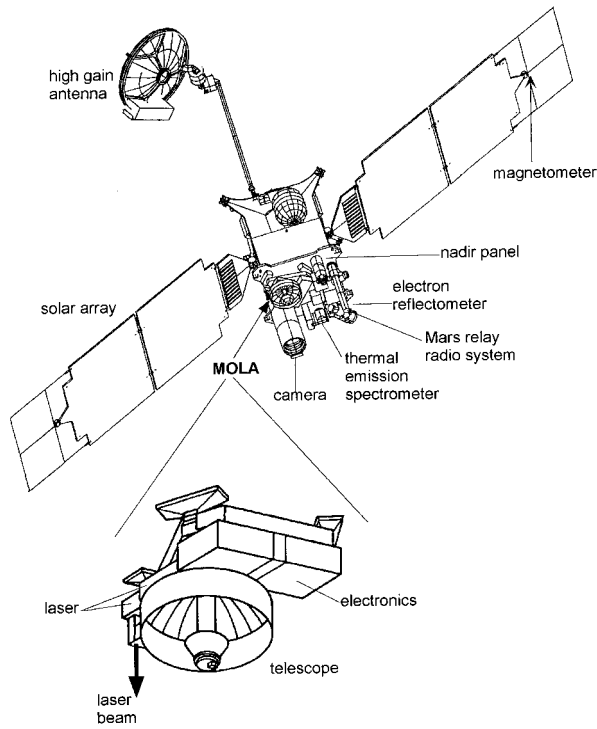
Fig. 1.   MGS spacecraft and the MOLA.

time-of-flight measurement.   Recently, Lemoine *et al.* showed that the MGS orbital position can be determined to an accuracy of 0.3 m radially and 1.7 m in total position, after the Mars gravity measurement data and improvement from the MOLA ground-track crossovers are incorporated.[6,7]   Usually the spacecraft position and pointing angle uncertainties are slowly varying random variables.   Therefore, the uncertainties in the relative topograph heights over local scale are determined primarily by the errors in the time-of-flight measurements.

In addition to measuring the laser-pulse time of flight, the MOLA also measures the transmitted and the echo laser-pulse energies and the echo pulse width at the threshold crossings.   The full echo pulse
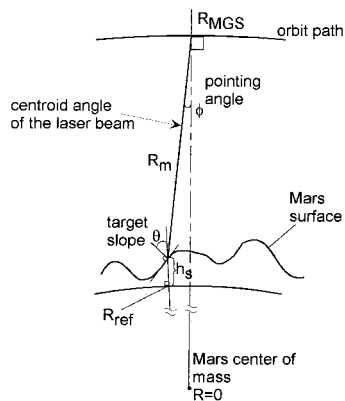
Fig. 2.   Illustration of the MOLA measurement geometry.   The drawing assumes that the pointing angle, the pointing error, and the surface normal vectors are all in the same plane.

energy and the root-mean-square (rms) pulse width can be determined as long as the echo pulse shape is known.

The apparent surface reflectivity can be determined from the detected pulse energy by use of the laser altimeter link equation:

$$E_r = E_{\mathrm{tr}}\tau_r \frac{A_r}{R_m{}^2} \frac{r_s}{\pi} \tau_a{}^2, \qquad (3)$$

where E_r is the echo pulse energy (joule), E_{tr} is the transmitted laser-pulse energy (joule), τ_r is the receiver optics transmission, A_r is the receiver telescope aperture area (square meters), r_s is the target surface reflectivity (assuming Lambertian), and τ_a is the one-way Mars atmosphere transmission.

The echo pulse width can be used to estimate the height variability that is due to surface slope and roughness within the laser footprint.   The surface slope of Mars is usually much larger than the spacecraft off-nadir pointing angle.   If roughness is neglected, the rms pulse width of the echo laser pulse is related to the surface slope as[8,9]

$$\langle \sigma_r{}^2 \rangle = (\sigma_x{}^2 + \sigma_f{}^2) + \frac{4R_m{}^2}{c^2}[\tan^4(\gamma) + \tan^2(\gamma)\tan^2(\theta)], \qquad (4)$$

where σ_x is the transmitted laser rms pulse width, σ_f is the rms receiver impulse response, and γ is the rms laser beam divergence angle (half-angle at the $1/\sqrt{e}$ intensity point).   The first term in the bracket of Eq. (4) accounts for the laser beam curvature and can often be neglected because usually $\gamma \ll \theta$.

The laser-pulse time of flight, the echo laser-pulse energy, and rms pulse width can be determined from the MOLA measurements by use of the procedures outlined in the remainder of this paper, assuming that the transmitted and the received laser-pulse shapes are Gaussian and that the instrument receiver is at its nominal operating temperature. Flight measurement data to date indicate that there have been no significant changes in the MOLA receiver characteristics since its prelaunch calibration.

2.   Laser Transmitter

The MOLA transmitter is a diode-laser-pumped, *Q*-switched, Cr:Nd:YAG slab laser.   The laser design details and a performance model are given in Ref. 10. The nominal transmitted pulse energy depends on temperature, and the pulse width is 8 ns full width at half-maximum (FWHM).   The laser beam full divergence angle was measured to be 0.42 mrad at the 90% encircled energy in the far field.   Assuming a Gaussian beam profile, the corresponding rms beam divergence angle was 0.093 mrad.

A small amount of the transmitted laser light is collected and coupled into the start pulse p-i-n photodiode through a multimode optical fiber.   The transmitted pulse energy is measured by the start pulse energy counter, which consists of a charge-to-time converter followed by an 8-bit counter.   A low-pass filter is used to broaden the pulse for the

Table 1. MOLA System Parameters

Symbol	Value	Description
E_{tr}	42 mJ	Nominal transmitted laser energy
λ	1064 nm	Laser wavelength
$FWHM_l$	8 ns	Nominal transmitted laser pulse width FWHM
θ_x	0.37 mrad	Laser beam full divergence angle at $1/e^2$ point (rms angle $\gamma = \theta_x/4$)
A_r	0.170 m^2	Receiver telescope entrance aperture area
θ_{FOV}	0.850 mrad	Receiver field of view
τ_r	0.565	Receiver optics transmission
$\Delta\lambda$	2.0 nm	Receiver optical bandwidth
η_d	0.35	APD quantum efficiency at 1064 nm
G	120	Average APD gain
k_{eff}	0.008	APD ionization coefficient ratio
I_{dk}	50 pA	APD bulk leakage current
N_{amp}	$(2.0 \text{ pA/Hz}^{1/2})^2$	Preamplifier input noise spectral density
R_{det}	1.26×10^8 V/W	Detector assembly responsivity
$\Delta t_0, \Delta t_1$	2.5 ns	TIU timing resolution
f	$99{,}996{,}311 \pm 2$ Hz	Master clock frequency (prior to MGS launch)

comparator circuit to trigger reliably. The filter has no effect on the total pulse area except for a fixed insertion loss. The threshold level for the transmitted pulse is fixed and can be changed only by ground command. The detailed calibration between the energy counter output and the actual transmitted laser-pulse energy is given in Ref. 11, which also includes the environmental effects such as the temperatures of the laser, the photodiode, and the related electronics.

The laser-pulse energy is a function of laser temperature and is also expected to decrease over the laser lifetime.[10] Because the pulse energy and width are correlated, the transmitted laser-pulse width in nanoseconds can be inferred from the pulse energy by the relationship[11]

$$FWHM_l = 326.62(E_l)^{-0.95} \text{ (ns)}, \tag{5}$$

where E_l is the transmitted laser energy in millijoules.

3. Mars Orbiter Laser Altimeter Receiver

The MOLA measurement timing diagram is shown in Fig. 3, and a simplified receiver block diagram is

$$\Delta T_{opt} = N/f + \Delta t_0 - \Delta t_1 - \tau_{le}(0) + \tau_f(0) + \tau_{le}(i) - \tau_f(i) - \tau_d(i)$$
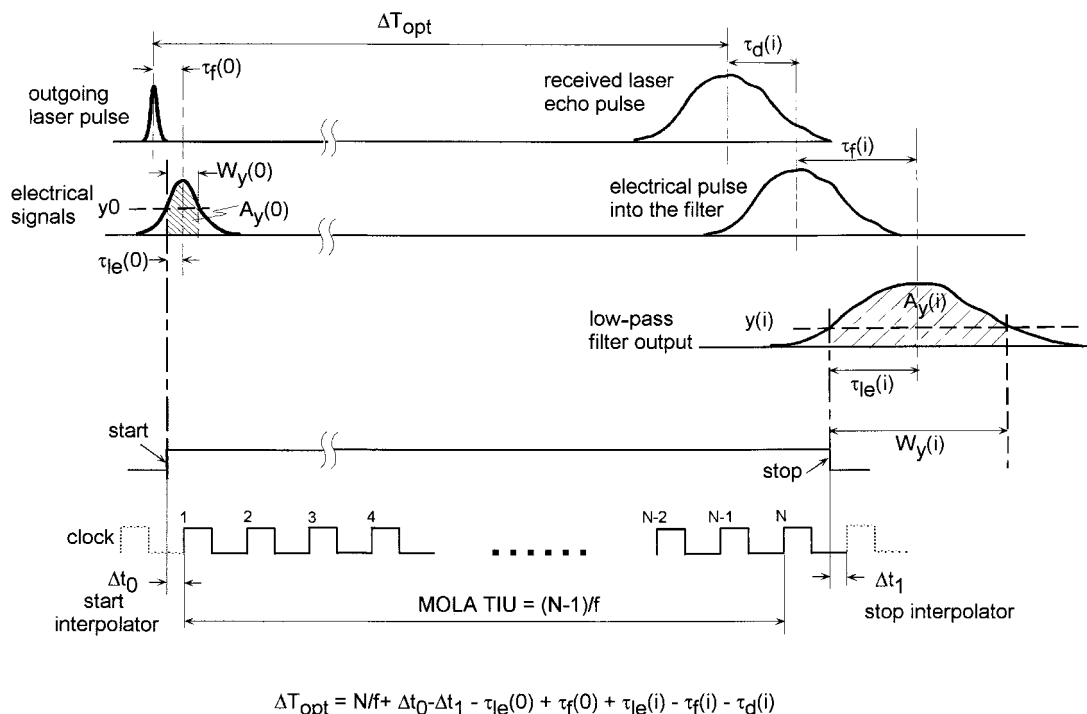
Fig. 3. Timing diagram of the MOLA optical and electrical signals.
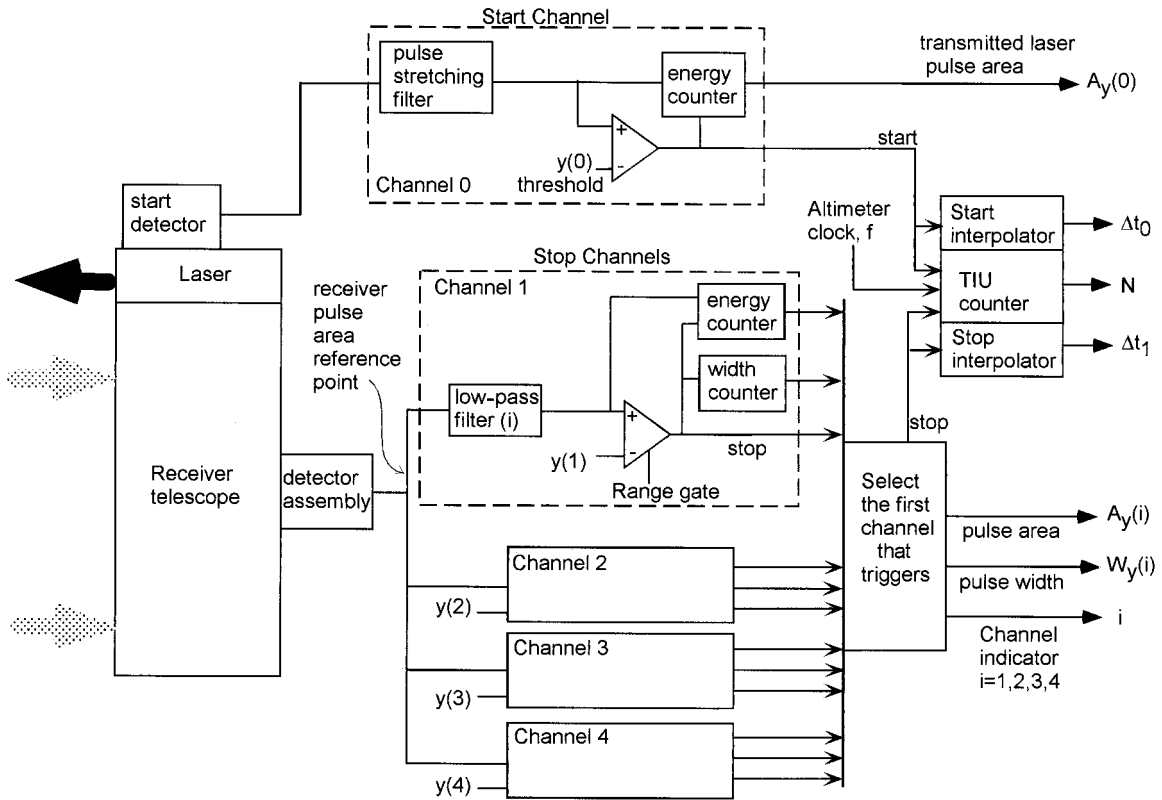
Fig. 4. Simplified MOLA receiver block diagram assuming lossless power splitter and filters and a unity scaling factor for all receiver channels.   The filter characteristics are listed in Table 2.

shown in Fig. 4.   Details of the MOLA optical system design are given by Ramos-Izquierdo *et al*.[12]   A detailed analysis of the characteristics of the laser altimeter receiver by use of a Si avalanche photodiode detector (Si APD) is given by Sun *et al*.[13]

The MOLA receiver contains a Si APD, a parallel bank of four electrical filters, and a time interval unit (TIU).[14]   We selected an analog filter-threshold crossing approach for the MOLA receiver as the only practical one given the power constraints of the receiver.   We also elected to use multiple receiver channels to accommodate the wide variability in the spreading of echo pulses.   The four receiver low-pass filters are a five-pole Bessel design, and their 3-dB bandwidths and impulse response are listed in Table 2.   The filter impulse response pulse shapes are closely approximated by Gaussian functions.   When the detected echo pulse shape is also Gaussian, the

receiver channel with the closest matching impulse response pulse width will have the highest signal-to-noise ratio (SNR) at the filter output.

The receiver threshold levels are automatically and independently adjusted by an algorithm in the flight computer to maintain a false-alarm rate of approximately 1% per channel.[15]   Each channel's threshold setting determines the minimum SNR required for that receiver channel to be triggered.   More than one channel can be triggered by the same echo pulse. However, only the channel with the shortest filter propagation delay will stop the TIU and have its measurement reported to the ground.   As shown in Fig. 3, the round-trip time of flight of the laser pulses measured at the start and echo pulse centroid points can be calculated from

$$\Delta T_{\mathrm{opt}} = \frac{N}{f} + \Delta t_0 - \Delta t_1 - \tau_{\mathrm{le}}(0) + \tau_f(0) + \tau_{\mathrm{le}}(i) - \tau_f(i)$$

$$- \tau_d(i). \qquad (6)$$

In Fig. 3 and Eq. (6), N is the TIU counter output (counts); f is the TIU clock frequency (hertz); Δt_0 is the start interpolator reading (seconds); Δt_1 is the stop interpolator reading (seconds), $i = 0$ represents the start pulse channel, and $i = 1, 2, 3, 4$ represents the receiver channel that was triggered; $\tau_{\mathrm{le}}(i)$ is the time from the leading-edge threshold crossing to the pulse centroid; $\tau_f(i)$ is the low-pass filter signal prop-

Table 2. Low-Pass Filter Parameters

Channel i	Impulse Width FWHM$_f(i)$ (ns)	Rms Width $\sigma_f(i)$ (ns)	Delay $\tau_f(i)$ (ns)	Noise Bandwidth B_n (MHz)
0	28.3	9.70	23.3	12.6
1	20	8.49	22	16.6
2	60	25.5	66	5.54
3	180	76.4	198	1.85
4	540	229	594	.615

agation delay; $\tau_d(i)$ is the receiver circuitry and cable delay; $A_y(i)$ is the pulse area between the pulse threshold crossings (volts times nanoseconds); $W_y(i)$ is the pulse width at threshold crossings (nanoseconds); and $y(i)$ is the effective threshold levels (volts).

4. Laser-Pulse Time-of-Flight Measurement

The time-of-flight measurements utilize the receiver's crystal oscillator, TIU, and start and stop interpolators. There is a timing offset because of the leading-edge triggering the TIU, which can be compensated for by use of the measured echo pulse width, pulse energy, and threshold level.

A. Time Interval Unit, Clock, and Time Base

The TIU consists of a binary counter that records the total number of clock pulses from the threshold crossings of the transmitted (start) pulse to the echo pulse. The clock consists of an oven-controlled crystal oscillator that has a frequency near 100 MHz and a short-term stability of 10^{-10} or better.[16]

The MOLA also records the time of the laser trigger pulse every 140 laser shots in reference to the spacecraft time base. These time stamps have a resolution of 1/256 s. We generated the laser trigger pulses by dividing the frequency of the MOLA clock. There is a 189.3 ± 0.5 μs delay from the laser trigger pulse to the laser-pulse emission time. The spacecraft's clock frequency is monitored on Earth through the spacecraft RF transmitter carrier frequency. The primary purpose of the laser-pulse time stamps is for use with the spacecraft orbit and pointing angle data to determine the along-track location of each laser footprint on the Mars surface.

The laser-pulse time stamps also serve to monitor the long-term aging and drift of the MOLA clock frequency during flight. We can estimate the MOLA clock period by averaging the time intervals between adjacent time stamps and dividing by the number of clock cycles elapsed between time stamps. The relative error in the estimate is bounded by the time stamp resolution, 1/256 s, divided by the total integration time over which the estimation is performed. The integration time for the MOLA mapping orbits was chosen to be 24 h. The absolute frequency of the MOLA clock was $99,996,311 \pm 2$ Hz before launch (March 1995). It has since drifted by -79 Hz or -0.8 parts per million at the beginning of the MOLA mapping phase in March 1999 and by another -19 Hz between March and September 1999.

B. Start and Stop Time Interpolators

To improve its range resolution, the MOLA timing electronics utilize identical interpolators for the start and the stop pulses. These allow determination of the threshold crossing times to approximately 0.25 of a clock period. Each interpolator utilizes three coaxial cables to delay the start or stop pulse by 0.25, 0.50, and 0.75 of a clock period. Each delayed pulse is then compared with the state of the clock with three AND gates and latches. The combination of the latched AND gate outputs determine which one of the

Table 3. Start Interpolator Bit Pattern to Time Conversion

Start Interpolator Bit Pattern	Median Time Offset Δt_0 (ns)	Interpolator Bin Width (ns)
00	1.1	2.2
01	3.6	2.8
10	5.9	1.8
11	8.4	3.2

delayed pulses was the closest to the subsequent clock transition. The results yield the time of the start and stop pulses with 0.25 clock period resolution. The instrument computer generates a 2-bit index of the start and the stop pulse latch settings, which determine the interpolator values. Because of the asymmetries in delays of the timing circuits, the actual interpolator values were not exactly 0.25 clock periods. The actual values were measured in the flight altimeter electronics subsystem tests, and their values are given in Tables 3 and 4.

C. Filter Characteristics

The start detector low-pass filter is a three-pole Bessel low-pass filter. Its bandwidth and other parameters are listed in Table 2, where it is designated as channel 0. The receiver low-pass filters are all a five-pole Bessel low-pass design, and the filter propagation delays are given by $\tau_f(i) \approx 1.10 \times \text{FWHM}(i)$. The receiver low-pass filter characteristics are listed in Table 2 as channels 1–4.

D. Corrections for Leading-Edge Timing

The threshold crossing times of the start and the stop pulses depend on the threshold level and the shape of the output pulse from the filter. To obtain an unbiased time-of-flight estimate, the optical pulse centroid should be used as the timing point on the start and the stop pulses. For symmetric pulses, the centroid point is equivalent to the pulse midpoint time. Therefore, the leading-edge timing correction is

$$\tau_{\text{le}}(i) = \frac{W_y(i)}{2}, \qquad (7)$$

where $W_y(i)$ is the measured width of the pulse in channel i.

Table 4. Stop Interpolator Bit Pattern to Time Conversion

TIU Counter Reading	Stop Interpolator Bit Pattern	Median Time Offset Δt_1 (ns)	Interpolator Bin Width (ns)
Even	00	0.9	1.8
Even	01	3.2	2.8
Even	10	5.5	2.6
Even	11	8.4	2.6
Odd	00	1.4	2.8
Odd	01	3.8	2.0
Odd	10	6.1	3.0
Odd	11	9.2	3.2

Table 5. Instrument Zero-Range Time Offsets with Leading-Edge Timing[a]

Channel i	Leading-Edge Time Offset (ns)	Estimated Pulse Width $W_y(i)$ (ns)	Instrument Time Bias $\tau_d(i)$ (ns)
1	36.9	40	43
2	54.7	93	43
3	106	230	31
4	343	480	−3

[a]Determined from the average daytime threshold level and the calculated instrument time bias.

Table 6. Pulse Width and Area Conversion Factors, Count Offsets, and the Threshold Scaling Factors

Channel i	$a_w(i)$ (ns/ count)	$b_w(i)$ (counts)	$a_A(i)$ (Vns/count)	$b_A(i)$ (counts)	$a_{\text{thre}}(i)$
1	3.60	7.4	0.411	2.3	2.29
	$(0.768)^a$	$(-10.5)^a$			
2	7.79	5.3	0.434	3.2	1.32
3	13.5	7.1	0.411	6.0	0.763
4	30.6	12.0	0.429	10	0.440

[a]If < 12 counts.

The timing correction for the start pulse is almost a constant because the laser energy and the width change relatively slowly over time, and the SNR at the input to the start discriminator is high. Because the start filter impulse response is much wider than the laser pulse, the start pulse width is dominated by the filter and is relatively insensitive to the pulse width variations. For example, if the transmitted laser-pulse width varies from 8 to 11 ns, the start pulse width output from the filter changes from 31.0 to 32.0 ns, and the variation in the correction for the leading-edge timing is less than 0.5 ns.

E. Instrument Time Bias

In addition to the filter propagation delays, there is also an instrument time (and range) bias that is due to electronics circuitry and cables. We determined the instrument time bias from a series of near-range measurements during ground tests, and it was taken to be the extrapolated time offset at zero range. The resultant range biases of the entire instrument with leading-edge timing and the measured pulse width at threshold crossings are given in Table 5. The unknown receiver delays can be solved by use of Eq. (6) with $\Delta T_{\text{opt}} = 0$ and $\tau_{\text{le}} = W_y(i)/2$. Because the width of the laser pulses was nearly constant in these tests, the start pulse width can be approximated by the FWHM pulse width, which is given by

$$W_y(0) \approx [\text{FWHM}_f(0)^2 + \text{FWHM}_l^2]^{1/2}, \qquad (8)$$

where $\text{FWHM}_f(0)$ is the filter impulse response pulse width given in Table 2, and the transmitted laser-pulse width is $\text{FWHM}_l \approx 8.0$ ns. The resultant receiver delay times are given in Table 5. The estimated echo pulse widths, $W_y(i)$, $i = 1, \ldots, 4$, are also listed. For convenience, the delay of the start pulse detection circuit was set to zero, and its effect was accounted for in the receiver channels.

5. Pulse Width, Area, and Energy Measurement

The MOLA receiver also measures the pulse width and area of the filtered echo pulse at the threshold crossings. The measured width and area depend on the threshold level, the filter impulse response, and the echo pulse shape. The optical echo pulse width and energy can be calculated given these measurements and the system parameters.

A. Pulse Width at the Threshold Crossings

Tests of the receiver electronics showed that the pulse width measured by the MOLA is given by

$$W_y(i) = a_W(i)[l(i) - b_W(i)], \quad i = 1, 2, 3, 4. \qquad (9)$$

Here $l(i)$ is the pulse-width count reported by the MOLA for channel i; and $b_W(i)$ and $a_W(i)$ are the count offset and the conversion factor for channel i, respectively. These constants are given in Table 6, and they were determined during the altimeter electronics tests when an electrical pulse was used as the input signal.

Because of the speed limitations of the electronics, the channel 1 measured pulse widths deviate from a linear relationship for short widths. The receiver characterization showed that the channel 1 pulse-width measurement can be approximated by two linear equations that intersect at 17-ns (12 counts) pulse width, as listed in Table 6. The maximum number of 63 counts in the pulse-width counters sets the upper limits of the linear dynamic range to approximately 200, 450, 750, and 1600 ns for channels 1–4, respectively.

B. Pulse Area between Threshold Crossings

Tests of the pulse area circuits showed that the pulse area measured by the MOLA is given by

$$A_y(i) = a_A(i)[m(i) - b_A(i)], \qquad (10)$$

where $A_y(i)$ is the pulse area in volts times nanosecond, $m(i)$ is the MOLA-reported pulse area count, and $a_A(i)$ and $b_A(i)$ are the conversion factors and the count offsets for channel i. The conversion factors and the count offsets were determined during the altimeter electronics tests when a pulse generator was used as the input signal. The results are listed in Table 6.

C. Channel Gain and Threshold Scaling Factors

The threshold-level settings reported by the MOLA are those applied directly to the discriminators. Each receiver channel has a different gain so as to optimize the receiver dynamic range. To calculate the values for the effective thresholds shown in Figs. 3 and 4, we had to scale the actual threshold settings by the power splitter loss and the voltage gain factors

for each channel. The resulting effective threshold levels are given by

$$y(i) = a_{\text{thre}}(i)\text{th}(i), \tag{11}$$

where $\text{th}(i)$ is the actual MOLA threshold voltage level at channel i as reported in the data packet and $a_{\text{thre}}(i)$ is the scaling factor listed in Table 6.

D. Solving for the Pulse Parameters

Given the MOLA measurements, the laser echo pulse width and the energy before the threshold crossing circuits can be determined if the pulse shape is known. For a Gaussian input and Gaussian filter impulse response, the output pulse shapes from the low-pass filter are also Gaussian and can be written as

$$f_i(t) = \frac{A}{\sqrt{2\pi}\sigma_r(i)} \exp\left[-\frac{t^2}{2\sigma_r(i)^2}\right]. \tag{12}$$

Here A is the pulse area and $\sigma_r(i)$ is the rms width, and we set the time origin to zero for convenience. The MOLA-measured pulse width $W_y(i)$ and the threshold level $y(i)$ are related by

$$y(i) = f_i\left[\frac{W_y(i)}{2}\right] = \frac{A}{\sqrt{2\pi}\sigma_r(i)} \exp\left\{-\frac{\left[\frac{W_y(i)}{2}\right]^2}{2\sigma_r(i)^2}\right\}. \tag{13}$$

The MOLA-measured pulse area between the threshold crossings is given by

$$A_y(i) = \int_{-W_y(i)/2}^{W_y(i)/2} \frac{A}{\sqrt{2\pi}\sigma_r(i)} \exp\left[-\frac{t^2}{2\sigma_r(i)^2}\right] dt$$
$$= A\, \text{erf}\left[\frac{W_y(i)}{2\sqrt{2}\sigma_r(i)}\right], \tag{14}$$

where $\text{erf}(x)$ is the standard error function.

We can solve for the rms pulse width by taking the ratio of Eqs. (14) and (13) and eliminating A, yielding

$$\frac{A_y(i)}{y(i)} = \frac{W_y(i)\sqrt{\pi}}{2} \frac{\text{erf}\left[\frac{W_y(i)}{2\sqrt{2}\sigma_r(i)}\right]}{\frac{W_y(i)}{2\sqrt{2}\sigma_r(i)} \exp\left\{-\left[\frac{W_y(i)}{2\sqrt{2}\sigma_r(i)}\right]^2\right\}}. \tag{15}$$

This can be simplified to

$$\frac{A_y(i)}{y(i)W_y(i)} = z\left[\frac{W_y(i)}{2\sqrt{2}\sigma_r(i)}\right]. \tag{16}$$

Here the function

$$z(x) \equiv \frac{\sqrt{\pi}}{2} \frac{\text{erf}(x)}{x\exp(-x^2)} \tag{17}$$

is a monotonically increasing function with a unique inverse function.
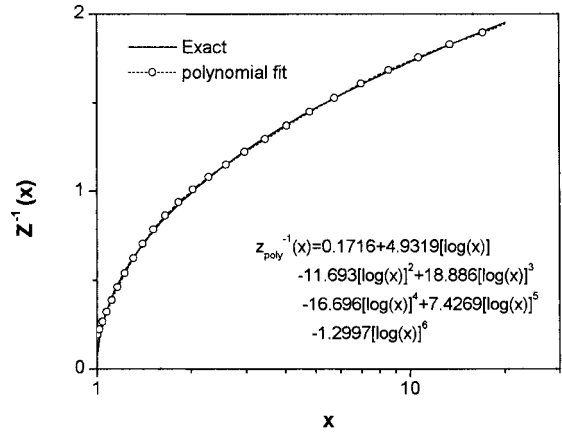
Fig. 5. Original and seventh-order polynomial fit of the inverse z function.

The rms pulse width $\sigma_r(i)$ can be solved for as

$$\sigma_r(i) = \frac{W_y(i)}{2\sqrt{2}} \frac{1}{z^{-1}\left[\frac{A_y(i)}{y(i)W_y(i)}\right]}. \tag{18}$$

Similarly, the full pulse area can be solved as

$$A = A_y(i) \frac{1}{\text{erf}\left\{z^{-1}\left[\frac{A_y(i)}{y(i)W_y(i)}\right]\right\}}. \tag{19}$$

The inverse function $z^{-1}(x)$ can be obtained by use of the standard numerical methods or curve fitting. The value of interest is $0.23 < z^{-1}(x) < 1.8$, which corresponds to the practical range of threshold values between 3 and 96% of the pulse amplitude. Figure 5 shows a plot of $z^{-1}(x)$ and a seventh-order polynomial curve fit to it.

E. Echo Pulse Width and Energy

The prior results can be used to solve for the energy and width of the MOLA echo pulses. Because the receiver electrical bandwidth is limited primarily by the low-pass filter in each channel, the detected pulse shape can be assumed unchanged up to the filters. The low-pass filters spread the pulse but preserve the pulse energy. For Gaussian input pulses, the rms pulse width of the echo laser pulse can be solved for as

$$\sigma_{\text{opt}} = [\sigma_r^2(i) - \sigma_f^2(i)]^{1/2}, \tag{20}$$

where the rms pulse widths of the filters are related to the FWHM impulse response pulse width in Table 2 by

$$\sigma_f(i) = \frac{\text{FWHM}(i)}{2[2\ln(2)]^{1/2}}. \tag{21}$$

Finally, we can solve for the optical energy of the echo pulse by dividing the full pulse area by the detector assembly responsivity, yielding

$$E_r = \frac{A}{R_{\text{det}}}. \quad (22)$$

During preflight testing, the detector responsivity was measured to be $R_{\text{det}} = 1.26 \times 10^8$ V/W at room temperature.

The detector responsivity can also be expressed in volts per detected photons (i.e., photoelectrons) per second, as

$$R_{\text{ph}} \equiv R_{\text{det}} \frac{hc}{\lambda \eta_d}, \quad (23)$$

where η_d is the photodetector quantum efficiency, h is Planck's constant, and λ is the laser wavelength.

6. Measurement Error Analysis

The errors in the MOLA measurements depend on the signal energy, pulse width, background level, and detector noise. These errors are summarized in the following subsections.

A. Variance of Time-of-Flight Measurement

The accuracy of the time-of-flight measurements depends on the echo pulse energy, pulse width, and noise level. Under normal conditions, the jitter of the start pulse threshold crossing times is much less than that for the echo pulses. For the timing jitter analysis for these cases, the time of flight measured by the MOLA, Eq. (6), can be simplified to

$$\Delta T_{\text{opt}} \approx t_r + \frac{W_y}{2} + T_o + \epsilon_Q$$

$$= \frac{t_r + t_f}{2} + T_o + \epsilon_Q, \quad (24)$$

where t_r and t_f are the receiver threshold crossing times at the pulse rising and falling edges, $W_y = t_f - t_r$ is the measured pulse width at the threshold crossings, T_o is a constant timing offset that accounts for all the filter and electronics delays and the start pulse centroid corrections, and ϵ_Q is the quantization error that is due to the TIU and pulse-width counter resolutions. To simplify the notation, the index of triggering channel numbers has been omitted.

Assuming that the errors in the threshold crossing times and those that are due to quantizations are all statistically independent, we can write the variance of the measured laser-pulse time of flight as

$$\text{var}(\Delta T_{\text{opt}}) = \text{var}\left(\frac{t_r + t_f}{2}\right) + \text{var}(\epsilon_Q)$$

$$= \frac{1}{4}\left[\text{var}(t_r) + \text{var}(t_f)\right]$$

$$+ \frac{\Delta t_0{}^2}{12} + \frac{\Delta t_1{}^2}{12} + \frac{\Delta W^2}{12}, \quad (25)$$

where Δt_0, Δt_1, and ΔW are the step sizes of the start and stop interpolators and the echo pulse-width counters. For MOLA, $\Delta t_0 \approx \Delta t_1 \approx 2.5$ ns, and the pulse-width step size ΔW is given as $a_W(i)$ in Table 6.

We can determine the variances of the echo pulse threshold crossing times $\text{var}(t_r)$ and $\text{var}(t_f)$ by adapting the derivation by Davidson and Sun.[17] The signal output from the receiver low-pass filter can be written as the sum of an average echo signal plus a random fluctuation noise as

$$x(t) = s(t) + n(t), \quad (26)$$

with $s(t) = \langle x(t) \rangle$ and $n(t) = x(t) - \langle x(t) \rangle$. The average signal can be approximated by the first two terms of its Taylor series expansion about the average leading-edge threshold crossing time as

$$s(t) \approx s(T_r) + s'(T_r)(t - T_r), \quad (27)$$

with the average threshold crossing time $T_r = \langle t_r \rangle$. Substituting approximation (27) into Eq. (26) and letting $t = t_r$, we obtain

$$x(t_r) \approx s(T_r) + s'(T_r)(t_r - T_r) + n(t_r). \quad (28)$$

At the threshold crossing, $x(t_r) \equiv s_{\text{th}}$ where s_{th} is the threshold level. Averaging both sides of approximation (28), we obtain $s(T_r) \equiv s_{\text{th}}$. As a result, the actual threshold crossing time and the noise are related by

$$s'(T_r)(t_r - T_r) + n(t_r) \approx 0. \quad (29)$$

The variance of threshold crossing time can now be written as

$$\text{var}(t_r) = \langle (t_r - T_r)^2 \rangle \approx \frac{\text{var}[n(T_r)]}{[s'(T_r)]^2}. \quad (30)$$

Note that $\text{var}[n(T_r)]$ and $\text{var}(t_r)$ are functions of the average threshold crossing time which is a function of the threshold level, the echo-pulse amplitude, and the pulse shape.

To obtain the derivatives of the signal, the output from the receiver low-pass filter can be modeled as a filtered Poisson point process. The average signal in terms of the detected photons per second can be written as[18]

$$s(t) = N_{\text{pe}} \int_{-\infty}^{\infty} h_f(\tau) p(t - \tau) \mathrm{d}\tau, \quad (31)$$

where $h_f(t)$ is the receiver low-pass filter impulse response and $p(t)$ is the normalized received optical pulse shape, which satisfies $\int_{-\infty}^{\infty} h_f(t)\mathrm{d}t = 1$ and $\int_{-\infty}^{\infty} p(t)\mathrm{d}t = 1$.

Both the echo pulse shape and the low-pass filter impulse response can be assumed as Gaussian with zero mean and with a rms pulse width of σ_{opt} and σ_f, respectively. Under this assumption, the output pulse shape given in Eq. (31), is also Gaussian with a rms pulse width $\sigma_r = (\sigma_{\text{opt}}^2 + \sigma_f^2)^{1/2}$. The derivative

of the average signal from the low-pass filter can be written as

$$s'(t) \approx N_{\text{pe}} \frac{t}{\sqrt{2\pi}(\sigma_{\text{opt}}^2 + \sigma_f^2)^{3/2}} \exp\left[\frac{-t^2}{2(\sigma_{\text{opt}}^2 + \sigma_f^2)}\right].$$

(32)

For Gaussian pulses, the average threshold crossing time is given by

$$T_r = -\sigma_r \left[2 \ln\left(\frac{\sqrt{2\pi}\sigma_r s_{\text{th}}}{N_{\text{pe}}}\right)\right]^{1/2},$$

(33)

where s_{th} is the threshold level in terms of detected photons per second. Note that the ratio of the threshold crossing time to the rms pulse width depends only on the ratio of the threshold level to the pulse amplitude. The threshold level s_{th} is related to the effective voltage threshold level of Fig. 3 by

$$s_{\text{th}} = \frac{y}{R_{\text{ph}}},$$

(34)

with R_{ph} given in Eq. (23).

The variance of the total noise in Eq. (30) can be written as the sum of the variances of shot noise that is due to the detected signal, the background radiation, and the detector dark current, as well as the preamplifier noise, i.e.,

$$\text{var}[n(t)] = \text{var}[n_{\text{sig}}(t)] + \text{var}(n_{\text{bg}}) + \text{var}(n_{\text{dk}}) + \text{var}(n_{\text{amp}}).$$

(35)

The variance of the shot noise that is due to the signal is given by[18]

$$\text{var}[n_{\text{sig}}(t)] = FN_{\text{pe}} \int_{-\infty}^{\infty} h_f^2(\tau) p(t - \tau) d\tau,$$

(36)

The variance of shot noise that is due to the background light can be written as[20]

$$\text{var}(n_{\text{bg}}) = 2F \eta_d \frac{\lambda}{hc} P_{\text{bg}} B_n,$$

(38)

where P_{bg} is the background light power that illuminates the detector and B_n is the one-sided filter noise bandwidth given by

$$B_n = \frac{1}{2} \int_{-\infty}^{\infty} h_f^2(\tau) d\tau.$$

(39)

The background light power can be calculated as

$$P_{\text{bg}} = I_s \Delta\lambda \frac{\theta_{\text{FOV}}^2}{4} r_s A_r \tau_r,$$

(40)

where $I_s = 0.311$ W(m^2/nm) is the average solar irradiance at 1064 nm at Mars; $\Delta\lambda$ is the receiver optical bandwidth; θ_{FOV} is the receiver FHWM field of view; and τ_r, r_s, and A_r are the same as in Eq. (3).

In a similar fashion, the variance of the shot noise from the detector dark current can be written as

$$\text{var}(n_{\text{dk}}) = 2F \frac{I_{\text{dk}}}{q} B_n,$$

(41)

where I_{dk} is the detector bulk dark current and q is the electron charge.

The variance of the detector preamplifier noise can be written as

$$\text{var}(n_{\text{amp}}) = \frac{I_{\text{amp}}^2 B_n}{q^2 G^2},$$

(42)

where I_{amp}^2 is the equivalent input noise current spectral density of the preamplifier in A^2/Hz.

Substituting Eqs. (36)–(42) into Eq. (35) and then substituting approximation (32) and Eq. (35) into Eq. (30), we can write the variance of the leading-edge threshold crossing time as

$$\text{var}(t_r) = \frac{FN_{\text{pe}} \int_{-\infty}^{\infty} h_f^2(\tau) p(T_r - \tau) d\tau + 2F\left(\frac{\eta_d}{hc/\lambda} P_{\text{bg}} + \frac{I_{\text{dk}}}{q}\right) B_n + \frac{I_{\text{amp}}^2}{q^2 G^2} B_n}{\left\{N_{\text{pe}} \frac{t}{\sqrt{2\pi} (\sigma_{\text{opt}}^2 + \sigma_f^2)^{3/2}} \exp\left[\frac{-t^2}{2(\sigma_{\text{opt}}^2 + \sigma_f^2)}\right]\right\}^2}.$$

(43)

where F is the detector excess noise factor defined as $F = \langle g_d^2 \rangle / \langle g_d \rangle^2$ and g_d is the photodetector multiplication gain. The Si APD used as the photodetector for the MOLA has an excess noise factor given by[19]

$$F = k_{\text{eff}} G + \left(2 - \frac{1}{G}\right)(1 - k_{\text{eff}}),$$

(37)

where k_{eff} is the ionization coefficient ratio and $G = \langle g_d \rangle$ is the average APD gain. For the MOLA Si APD, $k_{\text{eff}} \approx 0.008$ and $G \approx 120$.

Under the assumption of Gaussian pulse shapes, the average threshold crossing times at the rising and trailing edge are symmetric: $T_f = -T_r$, $N_{\text{sig}}(T_r) = N_{\text{sig}}(T_f)$, $s'(T_f) = -s'(T_r)$, and

$$\text{var}(t_r) = \text{var}(t_f).$$

(44)

We can obtain the variance of the time-of-flight measurement by substituting Eqs. (43) and (44) into Eq. (25). Plots of the MOLA timing errors versus signal level, surface slope, threshold level, and range to Mars are described in Subsection 6.D.

Gardner[8] has shown the lower bound on the variance of the time-of-flight measurement to be

$$\text{var}(T_{\text{opt}}) \geq \frac{\sigma_{\text{opt}2}}{N_{\text{pe}}F}. \qquad (45)$$

This lower bound can be achieved with ideal detectors and circuitry under no background illumination by recording the entire detected waveform and calculating the time of the pulse centroid.

B. Pulse-Width Measurement Error

The variance of the pulse-width measurement at the threshold crossings is given by

$$\text{var}(W_y) = \text{var}(t_r - t_f) + \frac{\Delta W^2}{12}$$

$$= \text{var}(t_r) + \text{var}(t_f) + \frac{\Delta W^2}{12}. \qquad (46)$$

Compared with Eq. (25), the variance of the measured pulse width is roughly four times that of the time-of-flight measurement, i.e. $\text{var}(W_y) \approx 4\,\text{var}(\Delta T_{\text{opt}})$.

Note that the variance given above is for the signal-pulse width from the low-pass filter measured at the threshold crossings. The variance in the calculated rms laser echo pulse width given in Eq. (18) is, in general, larger but is bounded by

$$\text{var}(\sigma_{\text{opt}}) < 2.36\,\text{var}(W_y) \qquad (47)$$

for threshold values lower than 96% of the pulse amplitude $[z^{-1}(x) > 0.23]$.

C. Variance of the Pulse Area Measurement Error

The MOLA receiver measures the pulse area by integrating the received signal between the two threshold crossings. The integration can be treated as the sampled output of a boxcar integrator with the impulse response given by

$$h_A(t) = \begin{cases} 1, & T_r \leq t \leq T_f \\ 0, & \text{otherwise} \end{cases}. \qquad (48)$$

The output of the integrator can be modeled as a filtered Poisson random point process[18] with the filter being the cascade of the boxcar integrator and the low-pass filter of the channel under consideration, i.e.,

$$h_{fA}(t) = \int_{-\infty}^{\infty} h_f(t - u)h_A(u)\mathrm{d}u = \int_{T_r}^{T_f} h_f(t - u)\mathrm{d}u. \quad (49)$$

The variance of the pulse area measurement at the threshold crossings can be written, similarly to Eq. (36), as

$$\text{var}(A_y) = R_{\text{ph}}{}^2 F N_{\text{pe}} \int_{-\infty}^{\infty} \left[\int_{T_r}^{T_f} h_f(\tau - u)\mathrm{d}u \right]^2 p(-\tau)\mathrm{d}\tau$$

$$+ \frac{\Delta A^2}{12}, \qquad (50)$$
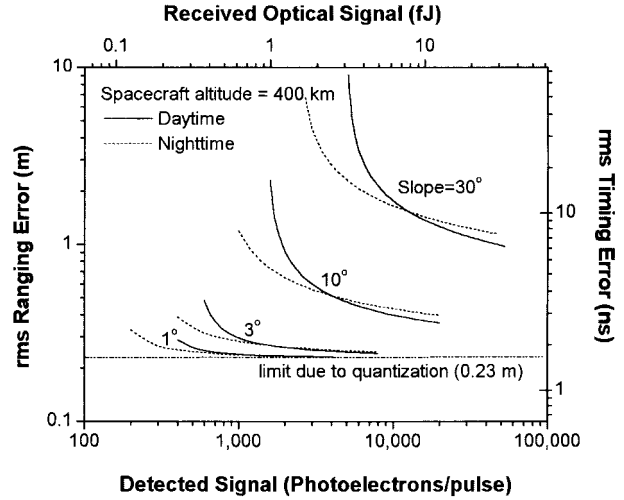
Fig. 6. MOLA channel 1 ranging error versus received signal level for 1-, 3-, 10-, and 30-deg slope surfaces.

where ΔA is the pulse area counter resolution given as $a_A(i)$ in Table 6.

If the width of the received optical signal pulse is much wider than the filter impulse response, then $\int_{T_r}^{T_f} h_f(\tau - u)\mathrm{d}u \approx 1$ for $T_r < \tau < T_f$, and

$$\text{var}(A_y) \approx R_{\text{ph}}{}^2 F N_{\text{pe}} \int_{T_r}^{T_f} p(-\tau)\mathrm{d}\tau + \frac{\Delta A}{12}$$

$$= R_{\text{ph}}{}^2 F N_{\text{pe}}' + \frac{\Delta A}{12}. \qquad (51)$$

N_{pe}' is the number of photoelectrons integrated between the threshold crossings and is given by $N_{\text{pe}}' = R_{\text{ph}}A_y$. Because the mean of the measured pulse area is given by $\langle A_y \rangle = R_{\text{ph}}N_{\text{pe}}'$, the normalized variance in pulse area can be written as

$$\epsilon_{Ay} = \frac{\text{var}(A_y)}{\langle A_y \rangle^2} \approx \frac{F}{N_{\text{pe}}'}, \qquad (52)$$

where the quantization error is neglected.

D. Calculated Performance for the Mars Orbiter Laser Altimeter

The MOLA system parameter values that are needed to calculate its measurement performance are listed in Table 1. The performance of channel 1 has been calculated from the analysis in this paper and the results are shown in Figs. 6–8.

Figure 6 shows the standard deviation (rms) of the ranging error versus the received signal level for various ground target slopes calculated with Eqs. (43) and (25). A nominal spacecraft altitude was assumed to be 400 km, and the threshold levels were $y = 0.275$ and $y = 0.137$ V for day and night backgrounds, respectively, which are close to on-orbit MOLA values. The ranging error increases rapidly at low signal levels because the threshold level is near the peak of the pulse where the slope is small.
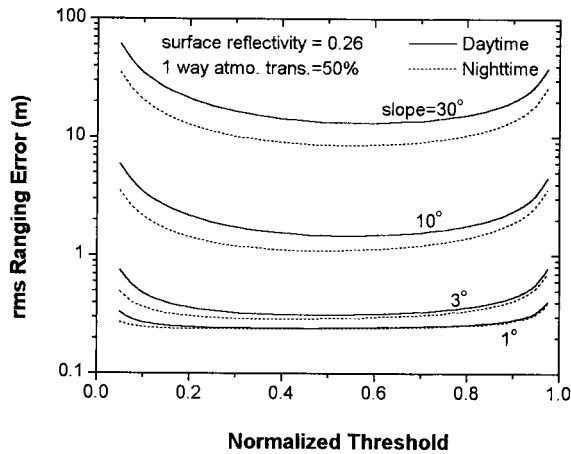
Fig. 7. MOLA channel 1 ranging error versus threshold level normalized with respect to pulse amplitude.

At high signal levels, the daytime ranging error is better than nighttime because the threshold level is roughly twice as high and closer to the optimal level. In the MOLA, the threshold levels are set to maintain a constant (~1%/channel) false-alarm rate rather than to minimize the ranging error.

The receiver sensitivity and performance of channels 2–4 are, in general, better than channel 1 for surfaces with larger slopes. Figure 6 also shows that the receiver quantization error is the dominating factor for a surface with small slopes. More-detailed analysis also shows that the error floor that is due to the receiver dark noise alone is approximately 30% the quantization error. Since the lower bound given by inequality (45) is roughly one third that of the leading-edge threshold crossing detection error given by Eq. (43), the MOLA error is approximately nine times the lower bound.

Figure 7 shows a plot of the rms ranging error versus the normalized threshold levels for 1-, 3-, 10-, and 30-deg slopes for a spacecraft altitude of 400 km. It shows that the range error is relatively insensitive to the threshold level as long as it is near the mid-

point of the echo pulse amplitude. However, the ranging error increases rapidly as the threshold is near the top or the bottom of the pulse waveform because of the small slopes of the signal waveform at the threshold crossing.
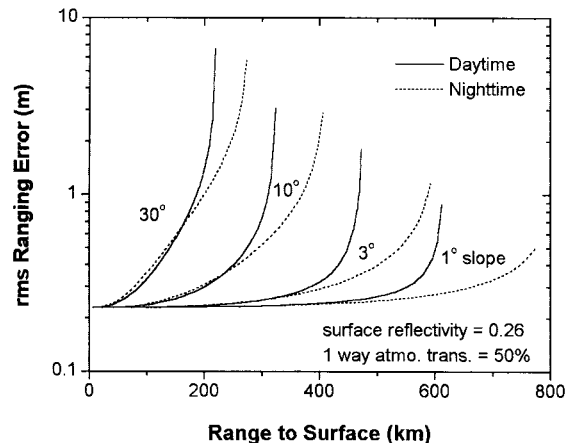
Figure 8 shows how the ranging error varies with ranging distance. It was particularly useful for our estimating the MOLA receiver performance during operation in elliptical orbits before the MGS spacecraft reached its final circular orbit around Mars. Note that both the signal level and the received pulse width in this case change with the spacecraft altitude according to Eqs. (3) and (4). It again shows that the ranging error increases rapidly as the echo signal level decreases to near the detection threshold. The echoes from a surface with larger slopes can still be detected by channels 2–4.

References

1. M. T. Zuber, D. E. Smith, S. C. Soloman, D. O. Muhleman, J. W. Head, J. B. Garvin, J. B. Abshire, and J. L. Bufton, "Mars Observer Laser Altimeter investigation," J. Geophys. Res. **97,** 7781–7797 (1992).
2. D. E. Smith, M. T. Zuber, H. V. Frey, J. B. Garvin, J. W. Head, D. O. Muhleman, G. H. Pettengill, R. J. Phillips, S. C. Solomon, H. J. Zwally, W. B. Banerdt, and T. C. Duxbury, "Topography of the northern hemisphere of Mars from the Mars Orbiter Laser Altimeter," Science **279,** 1686–1692 (1998).
3. M. T. Zuber, D. E. Smith, S. C. Solomon, J. B. Abshire, R. S. Afzal, O. Aharonson, K. Fishbaugh, P. G. Ford, H. V. Frey, J. B. Garvin, J. W. Head, A. B. Ivanov, C. L. Johnson, D. O. Muhleman, G. A. Neumann, G. H. Pettengill, R. J. Phillips, X. Sun, H. J. Zwally, W. B. Banerdt, and T. C. Duxbury, "Observation of the north polar region of Mars from the Mars Orbiter Laser Altimeter," Science **282,** 2053–2060 (1998).
4. A. A. Albee, F. D. Palluconi, and R. E. Arvidson, "Mars Global Surveyor Mission: overview and status," Science **279,** 1671–1672 (1998).
5. E. R. Cohen and B. N. Taylor, "The fundamental physical constants," Phys. Today **50,** Part 2, BG7–BG11 (1997).
6. F. G. Lemoine, D. D. Rowlands, D. E. Smith, D. S. Chinn, D. E. Pavlis, S. B. Luthcke, G. A. Neumann, and M. T. Zuber, "Orbit determination for Mars Global Surveyor during mapping," paper AAS99–328 presented at the AAS/AIAA Astrodynamics Specialist Conference, Girdwood, Alaska, 16–19 August 1999 (American Astronautical Society, Springfield, Va., 1999).
7. D. D. Rowlands, D. E. Pavlis, F. G. Lemoine, G. A. Neumann, and S. B. Luthcke, "The use of laser altimetry in the orbit and attitude determination of Mars Global Surveyor," Geophys. Res. Lett. **26,** 1191–1194 (1999).
8. C. S. Gardner, "Target signatures for laser altimeters: an analysis," Appl. Opt. **21,** 448–453 (1982).
9. C. S. Gardner, "Ranging performance of satellite laser altimeters," IEEE Trans. Geosci. Remote Sens. **30,** 1061–1072 (1992).

Fig. 8. MOLA channel 1 ranging error as a function of range.

10. R. S. Afzal, "The Mars Observer Laser Altimeter: laser transmitter," Appl. Opt. **33,** 3184–3188 (1994).

11. R. S. Afzal, "MOLA-2 laser transmitter calibration and performance," Technical report (Laser Remote Sensing Branch, NASA Goddard Space Flight Center, Greenbelt, Md., 1997).

12. L. Ramos-Izquierdo, J. L. Bufton, and P. Hayes, "Optical system design and integration of the Mars Observer Laser Altimeter," Appl. Opt. **33,** 307–322 (1994).

13. X. Sun, F. M. Davidson, L. Boutsikais, and J. B. Abshire, "Receiver characteristics of laser altimeters with avalanche photodiode," IEEE Trans. Aerosp. Electron. Syst. **28,** 268–274 (1992).

14. J. B. Abshire, S. S. Manizade, W. H. Schaefer, R. K. Zimmerman, J. S. Citwood, and J. C. Caldwell, "Design and performance of the receiver for the Mars Observer Laser Altimeter," in *Conference on Laser and Electro-Optics*, Vol. 10 of OSA Technical Digest Series (Optical Society of America, Washington, D.C., 1991), Paper CF14.

15. J. F. McGarry, L. K. Pacini, J. B. Abshire, and J. B. Blair, "Design and performance of an autonomous tracking system for the Mars Observer Laser Altimeter receiver," in *Conference on Laser and Electro-Optics*, Vol. 10 of OSA Technical Digest Series (Optical Society of America, Washington, D.C., 1991), Paper CThR27.

16. J. R. Vig, *Introduction of Quartz Frequency Standards*, Research and Development Technical Report, CECOM-TR-97-3 (Research, Development and Engineering Center, U.S. Army Communications-Electronics Command, Fort Monmouth, N.J., 1997).

17. F. M. Davidson and X. Sun, "Slot clock recovery in optical PPM communication systems with avalanche photodiode photodetectors," IEEE Trans. Commun. **37,** 1164–1172 (1989).

18. D. L. Snyder, *Random Point Process* (Wiley, New York, 1975).

19. P. P. Webb, R. J. McIntyre, and J. Conradi, "Properties of avalanche photodiodes," RCA Rev. **35,** 234–278 (1974).

20. R. G. Smith and S. D. Personick, "Receiver design for optical fiber communications," in *Semiconductor Devices for Optical Communication*, H. Kressel, ed. (Springer-Verlag, New York, 1980), Chap. 4.